האוניברסיטה העברית בירושלים
The Hebrew University of Jerusalem

The Faculty of Mathematics and Science,

Edmond Safra (Givat Ram) Campus,

Department of Chemistry.

Photodetachment cross section measurements for SF_6^- & SF_6^- based cluster anions

Thesis submitted for the degree of

“Master of Science”

In Physical Chemistry

Submitted by Maoz Nagler

ID: 021587019

Supervisor: Dr. Daniel Strasser

כסלו תשע"ה

December 2014

Acknowledgements

This work is dedicated to my parents, Ami and Yonat, and my wife, Sareet.

I would like to thank Itamar Luzon, Oded Heber and Daniel Strasser for their instruction, caring and patient.

Abstract

The following thesis deals with photodetachment cross section measurements of sulfur hexafluoride anion (SF_6^-) and small SF_6^- based cluster anions of the $(SF_6)_n^-$ and $(H_2O)_nSF_6^-$ form. SF_6^- photodetachment cross section curve shape as a function of photon energy in the 210-355nm and 420-705nm wavelength range is compared with a calculated cross section based on Frank-Condon overlaps of the initial SF_6^- anion ground state with energetically allowed final neutral states. By adding a shift of the adiabatic detachment energy (ADE) the calculated cross section successfully fits the data over 3 orders of magnitude cross section change as a function of photon energy. The fit to the measured cross section suggests an ADE value of ~ 1.7 ±0.02eV, significantly higher than the presently accepted ADE value of ~1eV. Small photodetachment cross section changes observed between SF_6^- and $(SF_6)_n^-$ with n=2,3 and 13 are discussed.

Table of Contents

1. Background

The work described in the following thesis explores the photodetachment of SF_6^-, small $(SF_6)_n^-$ cluster anions and $H_2O(SF_6)^-$. In addition to pure scientific research interest, sulfur hexafluoride is also used in many industrial applications. Its inertness and high cross section for electron attachment[2] make SF_6 an efficient electron scavenger commonly used in particle accelertires[1], electrical industry[3], plasma etching processing[4,5] and manufacturing of thin film transistor liquid crystal display.[6] Unfortunately, SF_6 has a negative environmental contribution as one of the most potent greenhouse gases released to the earth's atmosphere due to strong IR absorption[7] and long lifetime in Earth's atmosphere.[8] Interestingly, the dominant SF_6 destruction mechanism in the atmosphere is dissociative electron attachment.[8] Hence SF_6 atmospheric lifetime estimates depend strongly on the assumed cross-sections and electron density in the ionosphere, with estimates varying between 10000 years when neglecting dissociative electron attachment, and 400 years when assuming each collision event destroys the molecule.[8] Thus, the 100 years global warming potential of SF_6 is 23,900 higher than that of CO_2,[9] and SF_6 emissions to the atmosphere are monitored and were shown to grow from ~0.75Gg/yr to ~7.5Gg/yr between 1973 to 2008,[10] compatible with the reported growth of SF_6 sales.[11]

In spite extensive research efforts in the past two decades there is still ongoing debate about fundamental properties of the SF_6 molecule. The reported lifetimes of hot metastable SF_6^- anions that are formed by electron attachment vary by many orders of magnitude from 2μs to 1.1sec depending on experimental method.[18–21] Recent storage ring measurements with long storage times showed a non exponential decay of SF_6^- anions with $t^{-1.5}$, extending up to 2sec indicating that the unimolecular decay rate slows down as a function of time.[21] Another property that was vigorously explored is the adiabatic electron affinity (ADE). Experimental measurements report values between 0.55-1.20eV[13–16] while theoretical calculations also result in a wide range of electron affinities between 0.73-3.44eV.[12,17] In recent years, using kinetic modeling of hot SF_6^-

decay rates ADE values of ~1eV are generally accepted as recommended experimental values. [12] Similarly recent theoretical ADE estimates also converge to values around 1eV.[17,56]

The main experimental difficulty in $SF6^-$ ADE determination is the due to the fact that addition of an electron significantly changes the equilibrium S-F bond length from 1.56Å to 1.71Å.[22] Cosequently, as can be seen schematically in figure 1, the vertical electron detachment energy is shifted from the ADE to values of about 3.1eV.[23] Furthermore, as clearly shown in figure 1, only a small overlap exist between the neutral and anion ground states wave function, resulting in a vanishing probability of observing a direct transition at the adiabatic limit. Usually, photoelectron spectroscopy (PES) is a successful method for determining electron binding energies. Indeed, recent PES measurements of cold SF_6^- exhibit PES drop below the vertical detachment energy.[24] Furthermore, the PES exhibits unexpected double progression that inspired accurate structure calculations, which indicate that the SF_6^- anion departs from the previously assumed O_h symmetry of SF_6 and has a C_{4v} symmetry that can account for the observed PES features.[17] The elongated S-F bond length is about 1.9Å while the short S-F bond equilibrium is 1.6Å and the other four S-F bonds are about 1.70Å long.[17] Figure 1 shows the F.C. overlaps calculated by Eisfeld,[17] vanishing in the ADE limit. Furthermore, as shown in figure 1, the dissociation energy of SF_6 towards SF_5+F is about ~3.9eV.[25] On the other hand, SF_6^- dissociation energies towards SF_5^-+F and SF_5+F^- are ~1.44eV[12] and 1.75eV respectively,[29] which also lie in the range between the adiabatic detachment and vertical detachment energies. Consequently one can expect SF_6^- to exhibit interesting competition between detachment and dissociation following absorption of a photon. In the atmospheric chemistry context, detachment will return the system back to the neutral molecule, while dissociation will remove SF_6 from the atmosphere.

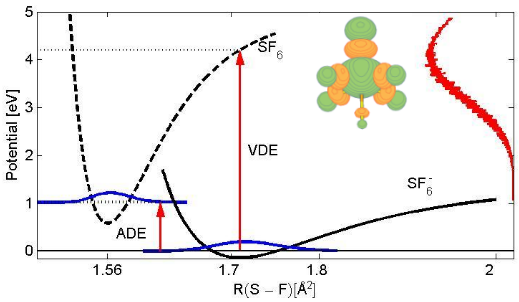

Figure 1: Schematic $\mathbf{SF_6}$ and $\mathbf{SF_6^-}$ potential curve shown respectively by the dashed and solid lines. Vibrational ground state functions are illustrated to emphasize the relativity large bind length shift and vertical arrows indicate the vertical and the adiabatic photodetachment processes. The red curve presents calculated relative FC overlaps of vibrationally excited neutral state with the anion ground state wave function, plotted as a function of photon energy. In the inset a suggested SF$_6^-$ structure with C_{4v} symmetry. Both the FC and the suggested structure are from Eisfeld calculations.[17]

I will now describe in detail and compare PES and Photo Detachment (PD) cross section measurements using a simplified harmonic oscillator model. In a PES experiment, a UV photon is absorbed by the ground state molecular anion and the energy spectrum of emitted photoelectron is recorded. The photon energy minus the measured electron kinetic energy can be related, by the energy conservation law, to the energy difference between the anionic ground state and excited neutral molecules:

(1) $$\Delta E = hv - E_k$$

Where ΔE is the difference between the neutral excited state energy and the anion ground state, hv is the photon energy and E_k is the electron kinetic energy.

Figure 2 shows a simplified one dimensional harmonic oscillator model demonstrating the PES measurement. When the Harmonic Oscillator (HO) equilibrium bond lengths are taken to be 1.56Å and 1.70Å for the neutral and anion respectively, the model ADE is 1eV and the vertical electron detachment energy is 3.1eV. Considering instantaneous photo-detachment from the anionic ground state to the free electron continuum, we can assume the nuclei do not have time to move. Accordingly, the relative probability of producing the different neutral vibrational states can be estimated by the Franck-Condon (FC) approximation, in which the transition probability is proportional to the square of the overlap integral of the initial and final vibrational wave functions, referred to as the FC factor:

(2) $$FC(v) = \left|\int_{-\infty}^{\infty} X_{v(R-R_0)}{}^{*} X_{0(R-{R_0}^{-})} dR\right|^2$$

Where R_0, R_0^- are the equilibrium bond lengths, and X_v(R) is the vibrational wave function of the *v* state as defined in equation 3:

(3) $$X_v(R) = \frac{1}{\sqrt{2^v v!}}\left(\frac{\mu\omega}{\pi\hbar}\right)^{\frac{1}{4}} e^{-\frac{m\omega R^2}{2\hbar}} H_v\left(\sqrt{\frac{\mu\omega}{\hbar}}R\right)$$

Where v is the vibration number, μ is the reduced mass of the nuclei, ω is the angular frequency of the harmonic oscillator and H_v are Hermit polynomials.

The calculated FC factor for the harmonic oscillator model is shown in figure 2 as a function of photon energy. As mentioned before, since the equilibrium bond length is shifted by 0.14Å, the overlap between the two ground states vanishes. On the other hand, the overlap reaches its maximal value, at the Vertical Detachment Energy (VDE): defined as the energy difference between the final and initial state equals to the potential curve difference at the SF_6^- equilibrium distance. The vibrational wavefunction, excited by VDE-ADE vibrational energy is illustrated in figure 2 shows the good overlap of the outer lobe of the excited vibrational state and the anion ground state, leading to maximal FC factor.

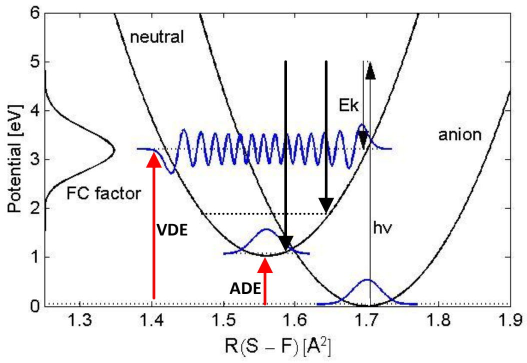

Figure 2: Photoelectron spectroscopy scheme of two harmonic oscillator potential, neutral and anion molecule. The success for transition between the anion to the neutral by using h*v* to vibrate is the FC overlap, which means that the bigger the FC is- the more chance the transition will happen.

On the other hand, in a PD cross section measurement the yield of all the neutral products is recorded as a function of photon energy. Therefore, as illustrated in figure 3, the total detachment probability at a given photon energy should be proportional to the sum over all FC factors of the energetically allowed final states, i.e., the states that lie below the energy of the absorbed photon.

(4) $$\sigma_{PD} \propto \sum_{v=0}^{v_{max}} FC(v)$$

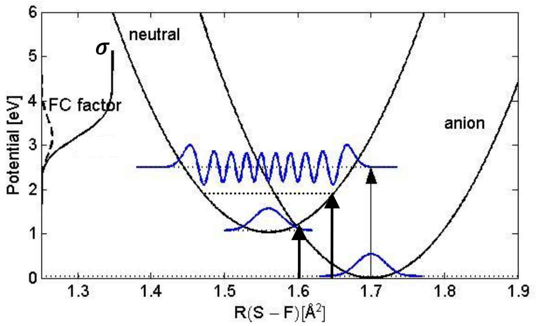

Figure 3: Approximation of neutral and anion potentials to harmonic oscillator (solid black), the ground states wave function (solid blue), a photon hit the anion molecule (solid arrow), detached an electron and the neutral fragment is measured. On the left side the normalized FC factor (dashed black) and the PD cross section (solid black) as a function of photon energy.

Considering only direct transitions, the PD cross section is therefore proportional to an integral over PES. However, PD cross section can also be affected by contribution from indirect detachment mechanisms. i.e. photoabsorption into an excited anion state (autodetachment resonance) followed by autodetachment as illustrated in equation 5.

(5) $$\begin{array}{l} SF_6^- + hv \longrightarrow SF_6 + e^-\ \textit{direct} \\ \quad\hookrightarrow SF_6^{-*} \longrightarrow SF_6 + e^-\ \textit{indirect} \end{array}$$

Analysis of electron attachment experiments,[27,28] and theoretical calculations,[29] indicate the existence of such excited SF_6^- states that may in principle contribute to the PD cross section in the relevant energy range between the vertical and adiabatic detachment energies. As opposed to the monotonously increasing PD cross section of a direct photodetachment mechanism illustrated in figure 4, indirect contribution can be expected to produce absorption resonances that will appear as a peak, corresponding F.C. overlap of the anion ground state with the autodetachmet resonance.

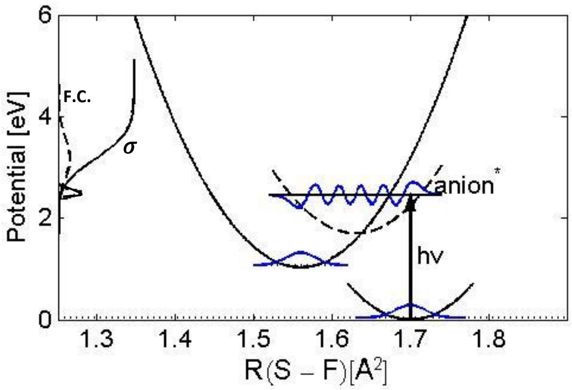

Figure 4: Indirect process and the ability of PD cross section to recognize it. If indeed there is an indirect process it will appear in the PD cross section spectrum.

Figure 5 shows a results from Itamar Luzon's M.Sc. work[54] of measured SF_6^- PD relative cross section compared with an integral over the SF_6^- PES adopted from Bopp *et al*[24]. Within the experimental errorbars, the PD cross section and integral over PES agree well and with no indication of contribution from indirect detachment. The large error bars at the lower energy in the spectrum derived from PES data, reflect the difficulty of observing direct transitions near the ADE limit in PES.

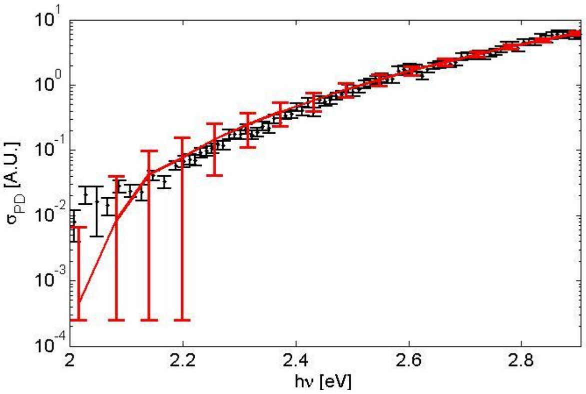

Figure 5: Comparing between the SF_6^- PD relative cross section (black dots) and the integral on SF_6^- photoelectron spectrum adopted from Bopp *et al*[24] (solid red).

Figure 6 shows the previously measured absolute PD cross section of SF_6^- as function of photon wavelength, reproduced from of Mock *et al.*[30] and Datskus et al [53]. The cross sections previously measured are in range of 300-390nm(=4.13-3.20eV) and 360-

395nm(=3.46-3.18eV) respectively, located near the VDE and far from the range explored in Itamar Luzon's M.Sc.

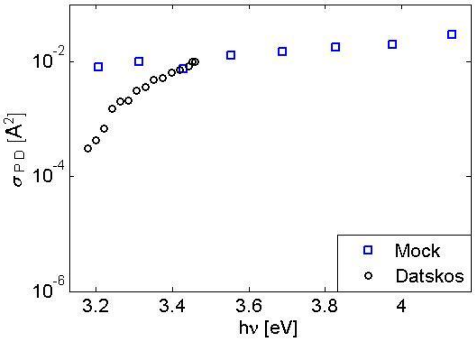

Figure 6: SF_6^- PD cross section by Mock[30] and Datskos.[53]

In my research I addressed SF_6^- based cluster anions. Although neutral $(SF_6)_n$ clusters are bound only by Van Der Waals forces, ionic species exhibit stronger binding energies due to the additional charge. For example, $(SF_6)_2^-$ is bound by ~100meV against dissociation.[61] Generally, clusters show lower binding energies with increasing cluster size, with the exception of "Magic number" clusters such as $(SF_6)_{13}^-$ that exhibits exceptional stability due to their icosahedral symmetry structure. [55,56,57]

For rare gas cation clusters, measurements established that the positive charge is delocalized over 3 rare gas atoms forming $Xe_n(Xe_3)^+$ in the case of Xe atoms.[33,34] If charge delocalization occurs also for the anionic $(SF_6)_n^-$ clusters, one can expect a dramatic change in the average S-F bond length which is known to be sensitive to the addition or removal of electron. In his M.Sc. thesis, Luzon showed that in an HO model system, the F.C. overlap and subsequently also the PD cross section can be extremely sensitive even to 0.01 Å change in the anion bond length as shown in figure 7.

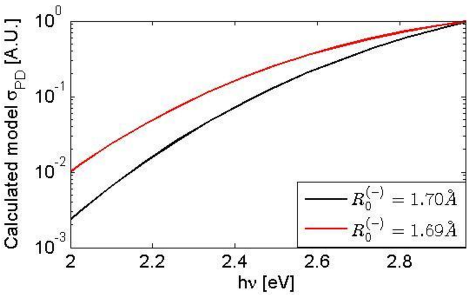

Figure 7: Normalized numerical calculation of PD relative cross section with a change of 0.01Å in equilibrium bond length, from 1.69Å (red) to 1.70Å (black).

In my M.Sc. project I first measured the SF_6^- relative PD cross section extending it from the 420-705 nm (=2.95-1.76eV) range covered by Itamar Luzon[54] also to the 300-400nm (=4.13-3.10eV) wavelengths. In this way enabling us to determine absolute PD cross section by normalizing to the measurements performed by Mock et al.[30] Furthermore, I measured the PD cross section of small cluster SF_6^- based anions of the $(SF_6)_n^-$ form, aiming to determine the effect of the interaction of the SF_6^- anion with the nearby neutral SF_6 molecules on its effective bond length. Finally, I present preliminary PD cross section of the $(H_2O)SF_6^-$ system, paving the way for future work on $(H_2O)_nSF_6^-$ systems that will explore H-bond effect on the SF_6^- system.

2. Experimental setup

Cold SF_6^- molecular anions formed in a pulsed supersonic expansion Even-Lavie ion source[35] are accelerated by 4.2keV potential and injected into a linear Electrostatic Ion Beam Trap (EIBT). [36–39] The fast ions are kept oscillating back and forth between two electrostatic mirrors, allowing us to isolate ions of specific charge over mass based on their oscillation frequency, to interrogate them by tunable wavelength laser and efficiently detect the neutral PD products. The main features of the EIBT setup are shown schematically in figure 8.

The EIBT is composed of two electrostatic mirrors, each mirror is made of 6 stainless still electrodes with controlled voltage which form a potential trap fast ions oscillating back and forth between the two mirrors, resembling an optical resonator. Every experimental cycle, a bunch of ions are injected into the EIBT by lowering the potential on the "entrance mirror" V_p electrode, making a hole in the mirror potential that allows ions to enter the trap. After the desired ions enter the trap, the V_p potential is raised and effectively traps the ions by closing the "hole" in the mirror. Under Ultra-High-Vacuum (UHV) conditions (typically10_{torr}^{-10}) ions can oscillate in the EIBT for times as long as 5 sec. [64] In order to synchronize the motion of specific ion species, a low RF voltage is applied to V_{RF} electrode. We typically use a 4V peak to peak sine wave at the oscillation frequency of the desired species that allows to synchronize the ion bunch to an external trigger and to keep the same ions mass from debunching due to their finite energy spread and trajectory differences. As the ion oscillation frequency is proportional to the$\sqrt{\mathrm{q/mass}}$, applying a synchronized periodic ±100 voltage pulse to a deflector electrode (labeled V_{KO} in figure 8) located inside the trap allows selecting a specific ion species by "kicking out" ions that oscillate at different frequencies.[40] Furthermore, a pickup ring electrode located near the center of the trap allows following the ions directly by observing the image charge induced on the pick-up electrode by the periodic passage of the charged particles[37,41]- A broader detailed explanation is given in section 4.2. Neutral products of the laser-anion interaction exit the ion trap and are detected on the MCP located downstream in a time delay after the laser pulse, corresponding to the velocity of the trapped ions and the product mass. A 3mm hole in the center of the MCP detector allows us to efficiently overlap the trapped ion beam with a co-linear laser beam of a pulsed tunable wavelength OPO laser[41].

The experiment is controlled by a specially designed Labview program allowing several days long measurement sessions, in which the computer continuously scans the laser wavelength and selected ion species to insure minimal systematic errors in the cross section measurements.

Thus by recording the yield of neutral products, number of anions and laser power as function of wavelength we are able to construct the PD cross section curve for each ion species, where the absolute scale normalization is done by comparison of SF_6^- PD cross section to Mock et al.[30]

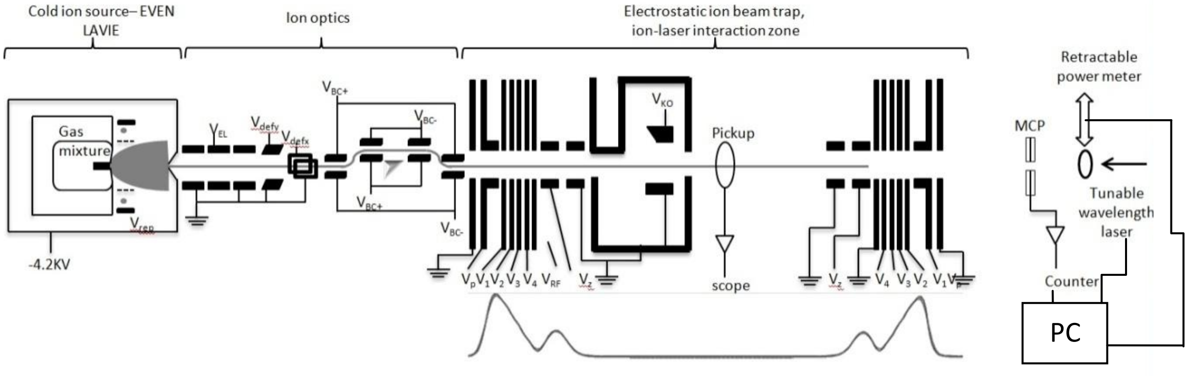

Figure 8: The experimental setup sketch. At the bottom is the typical potential (simulated) along the optical axis of the EIBT. The ion beam induced current measured by Pickup ring and the neutrals fragments are measured by a MCP in the end of the trap. Retractable power meter is measuring the laser power and programmed to do so for all wavelength once every eight rounds.

2.1. Ion source and ion optics

Molecular SF_6^- molecular anions and SF_6^- based cluster anions are generated in a supersonic expansion ion source located on a high voltage platform. The Even-Lavie pulsed valve releases short $\sim 22_{\mu s}$ pulses of a specially prepared gas mixture,[35] typically ~420 PSI Neon carrier gas, seeded by ~1% of SF_6 sample gas. When needed, few drops of water are introduced to the gas line mixing water vapor into the expanding gas mixture. The gas pulse supersonically expands into the "source" vacuum chamber that is pumped by a turbo pump to a background pressure of ~$5 \cdot 10^{-7}_{Torr}$. A pulsed circular electron gun accelerates 200eV electrons into the expanding gas, generating a variety of cations, anions as well as metastable neutral species. The rapidly expanding carrier gas cools down to temperatures as low as 10K,[35] leading to cooling and even clustering of the sample molecules and ions by multiple collisions with the expanding carrier gas. The supersonic expansion is skimmed by a 3mm skimmer located 100mm downstream of the pulsed valve to select the central coldest part of the expanding gas. After the skimmer, negatively charged species are accelerated by the potential drop from the -4.2kV high voltage platform at the source toward a grounded electrode located at the entrance of ion optics chamber. Thus, the source produces a pulsed beam of anions with a kinetic energy of $q \cdot 4.2KeV$, when q is the ion charge. As shown in figure 8, the source is followed by ion optics that include an Einzel lens as well as horizontal and vertical deflectors that focus and steer the ion beam into the EIBT with typical voltages of V_{EL}= 2.4KV with V_{defx}=28V, V_{defy}=30V. In addition, four pairs of "beam cleaner" electrodes (V_{BC+}=+1.032KV, V_{BC-}=-1.038) are pulsed to selectively guide ions arriving at the selected time along a chicane trajectory, while blocking neutral gas molecules as well as ion species with very different charge over mass ratio that arrive outside the selected time window. Figure 9 shows a typical single pass pickup signal[54], recorded while grounding the EIBT electrodes, resolving the charge over mass of the anionic species that we inject into the EIBT based on their time of flight from the ion source to the pickup electrode at the center of the trap. The most dominant peak belongs to SF_6^-, while the early shoulder is assigned to fragmentation into SF_m^- and the following peaks belong to $(SF_6)_n^-$ clusters. One can easily see that $(SF_6)_{13}^-$ peak, as befits "magic number" cluster, is higher than its neighbor's anions, reflecting its relative stability.

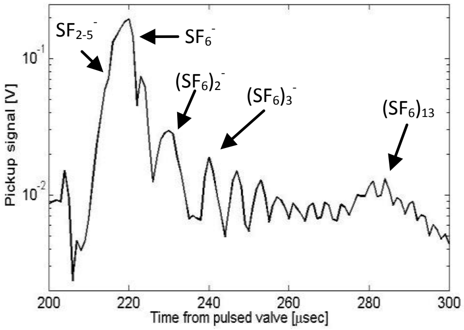

Figure 9: Pickup signal of ions that pass through the pickup. Anions of different $\sqrt{\mathbf{m/q}}$ pass the pickup electrode at different times, producing negative voltage peaks as a function of time. The highest peak (220ms) is a predominantly by SF_6^-, with an unresolved tail towards low TOF composed of SF_m^- with m ranging from 2-5. SF_6^- is followed by $(SF_6)_2^-$ $(SF_6)_3^-$ *etc.*, arriving respectively at 230µs, 240µs and longer times. The negative voltage indicates negative ions, and the amplitude is proportional to the number of ions.

2.2. Electrostatic ion beam trap (EIBT) , RF and Kick out

The EIBT and its different modes of operation were previously described in detail in a series of manuscripts by Daniel Zajfman, Daniel Strasser *and co-workers*.[36–39] A typical EIBT is made of two electrostatic mirrors and works similar to an optical resonator, supporting stable ion-trajectories that oscillate back and forth between two mirrors .The

EIBT is placed in an UHV chamber, pumped by a cryogenic pump typically to a pressure of 10^{-10}_{Torr} in order to minimize the loss of ions by collisions with the residual gas (RG). Each electrostatic mirror is made of a series of six negative electrodes with radial concentric symmetry that defines a smooth potential. The monotonically rising potential supplied to electrodes 1 - 4 (typically: V_1=-1.622kV, V_2=-3.247kV, V_3=-4.873kV and V_4=-6.5kV) produces a reflecting potential for the 4.2keV ion beam. While the focusing is provided by an Einzel lens, typically supplied with V_z=-3.2kV. The additional V_p electrode allows to either open or close the entrance mirror by setting V_p to-1.622kV or -4.42kV respectively. In order to trap a desired species, V_p is lowered to allow ions to enter the trap and is raised back once the desired species passes the pickup. For example: according to the assignments shown in figure 8, SF_6^- ions will be trapped by raising V_p 230µs after the pulsed valve while raising V_p at 245µs will trap $(SF_6)_3^-$clusters. The ions that are inside the EIBT at the time the mirror is closed are trapped, oscillating between the mirrors.[42] In addition, synchronized square 100V pulses (alternating between positive and negative voltages for technical reasons) are applied to V_{KO} during the first 100 oscillations, the deflector inside the EIBT and effectively "kick out" the majority of the ions oscillating out of synch with the desired ion species oscillating at the selected RF frequency[40]. Thus, we obtain a trapped ion bunch mass selected and synchronized to the laser pulse.

2.3. Laser

We are using an EKSPLA tunable wavelength Laser base on optical parametric oscillator (OPO) pumped by a ND-YAG laser.[41]At a repetition rate of 10Hz, the OPO provides ~4ns pulses with tunable wavelength. The OPO produced a computer controlled "Signal" wavelength in the range of $420-709nm\ (2.95-1.75eV)$, and a corresponding "Second Harmonic" (SH) in the $210-355nm\ (5.90-3.49eV)$ range. Each range of wavelength have a different output hole and their laser beam is further shaped and directed towards the EIBT by a telescope and a set of 3 mirrors that allow passing the laser beam through the 3mm hole in the MCP detector and overlapping it with the optical axis of the EIBT. Figure10 shows a typical measured output power of the OPO signal and SH as a function of photon energy. To allow long measurement sessions, laser power is monitored during the measurement every eight rounds of wavelength scans by using a computer controlled stepper motor power meter into and out of the beam, for measuring the laser beam behind 3mm iris at the entrance to the EIBT.

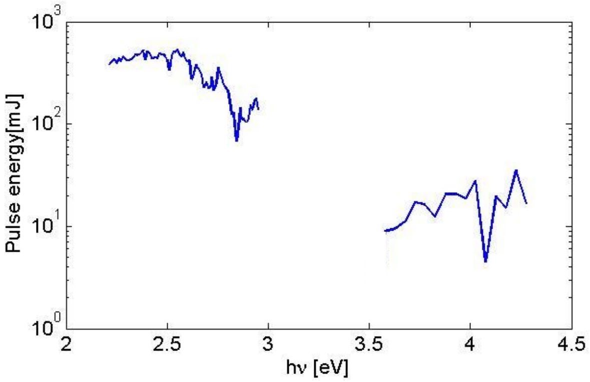

Figure 10: Typical laser pulse energy output from the OPO. The "Signal" range shown in the figure is 2.21-2.95eV and the "Second Harmonic" (SH) range shown in the figure is 3.53-4.28eV.

2.4. Timing and synchronizations

Figures 11a and 11b describe the timing scheme of a typical experiment of SF_6, showing the sequence of computer controlled triggers supplied to the experimental apparatus (each anion has different time sets). The experiment is synchronized to the laser pulse timing. The first timing signal triggers the pulsed valve, at t=0 which is ~60ms after the previous laser pulse. The delay from the laser pulse is calculated such that the next laser pulses (arriving at 40ms, 140ms, 240ms, 340ms, 440ms and 540ms) will hit the ion bunch when it is at the center of the trap and is moving towards the exit mirror. The neutral photodetachment products retain the parent ion velocity and move toward the MCP detector. The pulsed valve trigger is followed by a 10μs ionizer pulse, delayed by 69μs. The beam cleaner is typically activated after 208μs for 8μs. As shown in figure 8, SF_6^- anions reach the center of the EIBT at about 220μs and the EIBT entrance mirror is closed by switching the V_p at 230μs and keeping it high until the end of the cycle at which point remaining ions are released from the trap. Once the trap is closed, a synchronized sine wave is applied to the RF electrode. A periodic “kick out” pulse sequence is applied to the V_{KO} deflector electrode for ~200 oscillations and is delayed by a phase of 1.4π with respect to the RF sinewave. The phase shift is optimized for keeping the desired ion bunch, while kicking out all other species with a $\frac{\Delta m}{m} = 7 \cdot 10^{-3}$ mass resolution.[40] It is important to note that it is necessary to match the RF frequency to be an integer times the exact 9.9986Hz repetition frequency of the laser in order to synchronize the ion bunch with more than one laser pulse. For the different ions there are systematic changes in the timing scheme according to their charge over mass ratio. A critically important technical improvement was to introduce a 0.9998 compensation factor to match the nominal computer internal clock and the RF generator internal clocks.

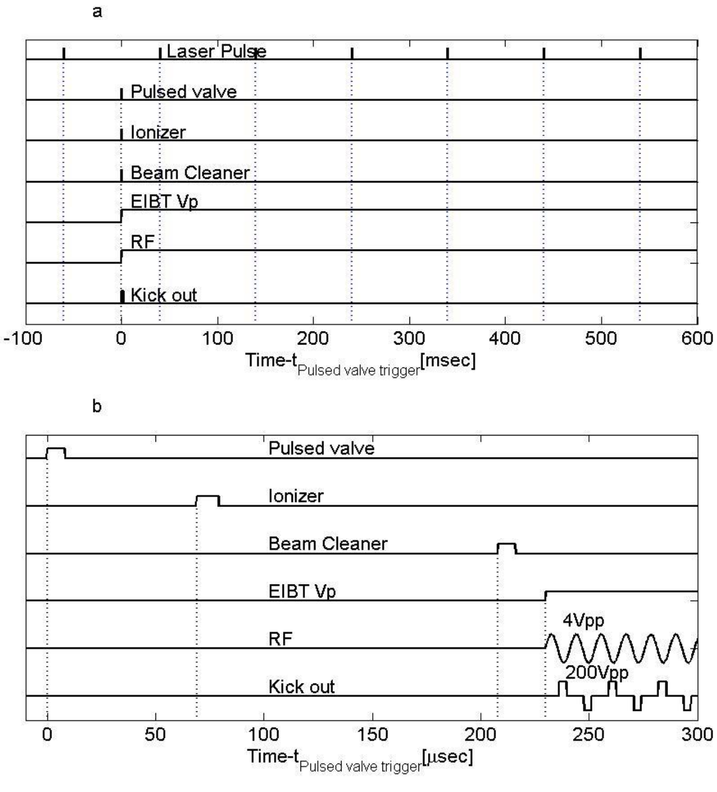

Figure 11: Experimental timing scheme for SF_6^-: a. Show synchronization between the laser to the setup triggers. After the first laser pulse, the pulse valve starts the sequence and there are six laser shots (blue dots) at time intervals of 100 ms that overlap with the trapped ions while the trapped ions synchronized toward the exit mirror.

b. Zoom in to the pulsed valve time zone, in order to see the different triggers. First, a gas is released from the pulsed valve for 8µs. After that, the gas get ionized for 10µs and then the ion beam is being cleaned from different masses, energies, and neutrals by the Beam Cleaner. Finally, the ions are trapped inside the EIBT by rising V_p and gets into resonance by the RFand the undesired anions inside the EIBT are mass selected and removed by the Kickout.

3. Data acquisition

As shown in figure 8, the ions and their neutral products are detected by two separate detectors: a multi channel plate (MCP)[43,44] that records the impact of neutral products of ion collisions with the residual gas and neutral products of ion interaction with the laser pulse. The pickup ring electrode that acts as an antenna, measuring the induced image charge of the ion bunch oscillating inside the EIBT.[38,45]

3.1. Neutral product detection

Neutral products of the ion beam interaction with residual gas collisions, blackbody radiation[47] and laser pulses are not deflected by the EIBT mirror. Neutrals that fly out of the exit mirror can hit the MCP detector located 67cm after the trap. Although such neutral products have no charge, their high kinetic energy is sufficient to produce a signal on the MCP detector. The small current peaks on the MCP anode are amplified and then discriminated by a constant function discriminator (CFD) producing a digital NIM timing signal, which is converted to a TTL signal and fed into a "NI-PCI-6602 DAQ" PC card that records the neutral products arrival times to the detector with 100ns time resolution, limitted by the maximal counter clock frequency. In order to avoid saturation of the acquisition electronics we limit the maximal count rates to 1 over 100ns by reducing the number of ions getting to the trap and beginning the measurement at 30ms trap time.

3.2. Capacitive pickup ion detection

The time evolution of the ion bunch shape is directly and non-destructively measured by a sensitive antenna ring electrode (pickup) that is slightly shifted from the center of the trap towards the exit mirror[42]. The pickup is connected to an amplifier and then to a dedicated scope that records the pickup signal during an entire trapping cycle with sampling frequency of 1MHz. The pickup electrode length is 7 mm and has an inner diameter of 18 mm. The total capacitance of the pick-up electrode, including its support rod and vacuum feed through is C∼10pF. Due to various slow potential drifts and noises in the lab it is not possible to determine precisely the induced DC charge from the measured voltage. However, the AC image charge induced by the passage of an ion bunch can be determined precisely as will be further explained in the data analysis section 4.2. In order to insure that the ions are all bunched an RF voltage of 10V is applied to the V_{RF} electrode of the trap, effectively bunching all the trapped same mass ions,[42] allowing us to neglect any DC contribution. We can therefore relate the number of ions in the trap to the area of a pulse produced by the ion bunch as it passes through the pickup.[42]

$$(6) \qquad N_{ions} = \frac{C}{L_p}\frac{v}{eq}A$$

Where Lp is the pickup length, and C in the capacitance, v is the ion velocity and A is the area under the oscillation.

From the same paper by Rahinov et al.[42] we see:

$$(7) \qquad A = const * T * Vpp$$

Where T is the time of oscillation and V_{pp} is the different between minimum and maximum in the oscillations and A is a const depending on trap geometry and RF voltage.

4. Data analysis

In the data analysis section it will be explained how the raw data is collected from the pickup and MCP is analyzed to derive the photodetachment cross section for a selected ion species as a function of photon energy.

$$(8) \qquad \sigma_{PD} = \frac{1}{F}\frac{N_{neut}}{N_{ions}}\frac{1}{\Phi_{\mathrm{laser}}}$$

Where N_{neut} represents the number of neutral photodetachment products, N_{ions} represents the number of anions and F is the geometric overlap of the laser beam in the ion bunch.

4.1. Measurement of the number of neutral photo-products

A histogram of neutral hit times detected on the MCP as a function of trapping time is shown in figure 12.The decaying background signal is caused by collisions of the ions with RG, while the spikes spaced by 100 ms, are due to laser photodetachment neutral products. Figure 13 shows a zoomed in view around the time of the first laser pulse. The sharp peak at t=0 is due to electronic noise arriving in coincidence with the firing of the laser pulse. For SF_6^- parent ions, neutral photo detachment products born at the center of the trap are expected to arrive in a time window between 8.6μs and 11.9μs after the laser pulse due to the time of flight (TOF) from EIBT to the MCP. Knowing the SF_6 based cluster anions velocity scales with $\sqrt{\mathrm{q/mass}}$, we derive arriving time windows of 12.16-16.83μs, 14.90-20.61μs, 31.01-42.91μs and 9.11-12.61μs for $(SF_6)_2^-$, $(SF_6)_3^-$, $(SF_6)_{13}^-$ and $(H_2O)SF_6^-$ respectably. The small tail visible in the log scale representation in figure 11 for all the anions is due to a negligible number of neutralization events that occur not in the field free region of the trap but in the mirror region that nevertheless arrive to the MCP and produce a measurable signal, albeit arriving with lower speed and at therefore at later times. The periodic background, which is typically more than 1000 times smaller than the photodetachment signal, is due to residual gas collisions and is modulated due to the oscillations of the ion bunch. Assuming that the decay of the ion beam occurs on long time scales we calculate the average background signal in one oscillation period, $N_{BG}(t)$, using 20 oscillations before and after the laser pulse. The periodic average background is then subtracted from the MCP signal, with a signal to noise level that for some ions is even better then $>10^4$. The averaged BG stayed the same before and after hit, implying negligible change had happened to the total number of ions inside the EIBT due to the laser pulse.

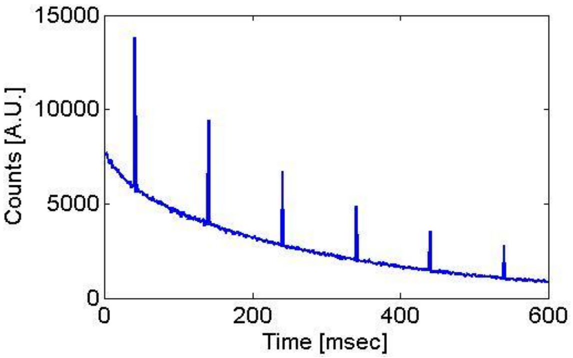

Figure 12: Life time of the neutrals fragments of $(SF_6)_2^-$ as detected by the MCP. The decay is due to residual gas collision while the spikes evolve due to laser noise and the laser-molecule overlap.

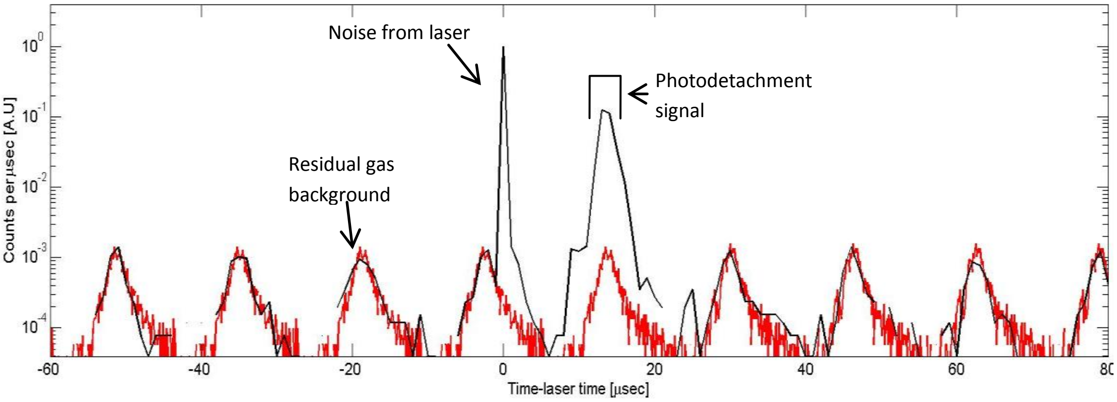

Figure 13: Zoom around the laser time for $(SF_6)_2^-$. The raw data is average of about ~1500 measurements (in black) and the averaged backgrounds from before and after the laser shot is shown (in red). After synchronization, the ions-laser photodetachment neutral signal (square marker) comes with the residual gas neutral signal. Notice that the number of ions in the EIBT did not change due to the laser shot.

In figure 14 we see the normalized ion bunches and the time windows for the different ion species. In data analysis, the time windows are used as a tool for cleaning the PD cross section spectra from possible contaminations in the desired ion sample. In some cases there are some overlaps between the times windows, but we saw it does not change the results since in each experiment we put an RF frequency for the specific measured ion and the other ions spread over and do not come as a sharp bunch.

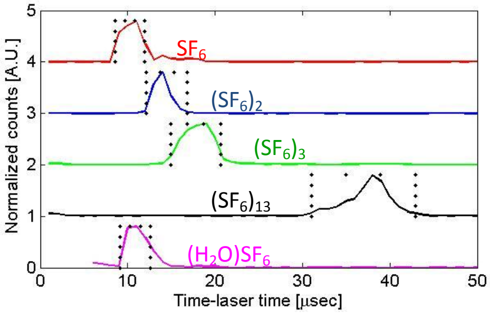

Figure 14: Normalized hits on the MCP in different heights with time windows (the area between the black dots on every cluster hits) for SF_6, $(SF_6)_2$, $(SF_6)_3$, $(SF_6)_{13}$, $(H_2O)SF_6$

4.2. Measurement of the number of ions in the trap (N_{ions})

Figure 15 shows frequency harmonics of $(SF_6)_2^-$ after doing Fourier Transform to the raw data and using square filter around the first harmonics of the ion frequency, already in the gathering of the data. The data shows the ion frequency and harmonics reflecting the shape of the ion bunch and pickup position. The mass is 292amu, the frequency is 61561.83Hz and the harmonics are 123123.66Hz (=61561.83*2), 184685.49Hz (=61561.83*3) etc.

Following reference[42] we can derive an analytical expression for the harmonics spectrum, assuming Gaussian bunch shapes of width Γ, by performing a Fourier transform on the periodic signal S(t):

$$(9) \qquad S(t) = A(t)\sum_{j=-\infty}^{\infty}\frac{1}{\sqrt{2\pi}\Gamma}\left(\exp\left(-\frac{(t-jT_0)^2}{2\Gamma^2}\right)+\exp\left(-\frac{(t-(j+\kappa)T_0)^2}{2\Gamma^2}\right)\right)$$

Where $A(t)$ is the time dependent area of each temporal peak corresponding to the decaying number of ions, j is the oscillation number and T_0 is the oscillation period. The expressions show two peaks for each oscillation: a forward and a backward pass through the pick-up with κ representing the relative location of the pickup in the trap. In our setup the pick-up is slightly removed from the center of the trap toward the exit mirror, corresponding to κ=0.4511. Equation 10 shows the derived peak intensity of each harmonic.

$$(10) \qquad S_n \propto \sqrt{2 + 2\cos(2\pi n\kappa)} \cdot \exp\left(-\frac{(n\Gamma/\mathrm{T}_0)^2}{2}\right)$$

Where n is the harmonic number, and S_n is the harmonic amplitude.

When looking at the cosine in the equation and noticing that $\kappa \sim \frac{1}{2}$ we can understand why the even harmonics in figure 15 are found to be higher than the odd harmonics.

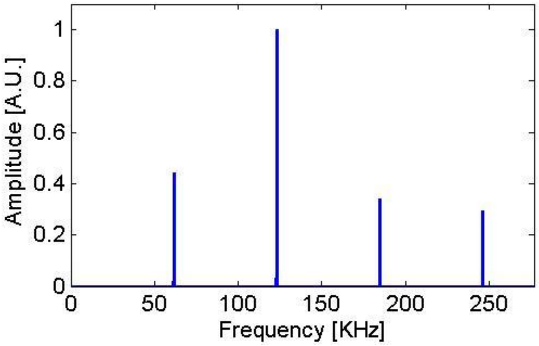

Figure 15: Fourier signal of $(SF_6)_2^-$ after square filter and 16 injections averages. This is able due to the phase lock by the RF. It is easy to see that the even harmonics are larger than the odd harmonics.

Figure 16 shows a zoom in on typical filtered pickup signal obtained by inverse Fourier transform. Note that since the image charge is of negative ions, the minima correspond to the ion bunch passing through the pickup and the maxima are when the ion beam is in one of the mirrors. The short and long half oscillations are clearly visible and it's due to the pickup location that is shifted slightly toward the exit mirror. We can therefore assign the times at which the ions are in the field free region moving towards the exit mirror. To capture the evolution of the number of ions as a function of time, we subtract the minima from the maxima signal and average the V_{pp} over every 200 oscillations. We found that for our experimental conditions gamma scales with the oscillation time of the ions and is equal to $\Gamma = 0.21\ T_0$.

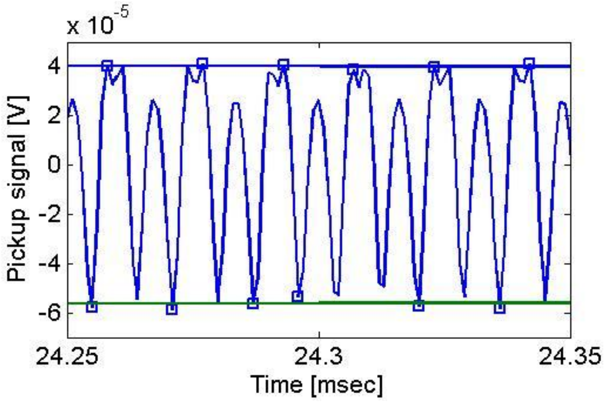

Figure 16: Clean pickup time signal of (SF$_6$)$_2^-$. It is easy to see the oscillation of the ion beam and the minimum points shows the time the ion bunch pass throw the pickup. The pickup is not located exactly in the middle of the EIBT and that's why one minimum point is dipper then it neighbor point, when the less dipper minimum points are when the ion bunch closer to the exit mirror. The number of ions in the EIBT is proportional to the difference between the green and blue lines.

As can be derived from equations 6 and 7:

$$(11)\ N_{ions} \propto V_{pp}$$

Figure 17 shows the resulting number of (SF$_6$)$_2^-$ ions in the EIBT for a typical trapping of desired ions.

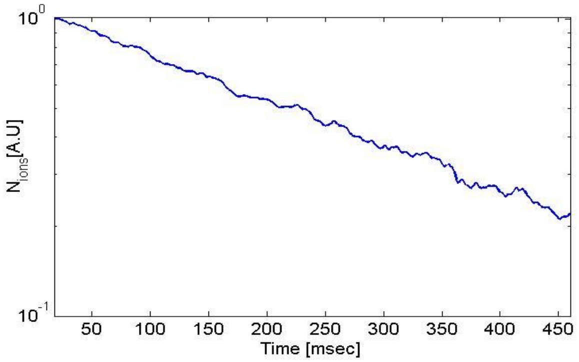

Figure 17: Number of (SF$_6$)$_2^-$ ions in the EIBT, exponentially decaying as a function of trapping time.

4.3. Calculating PD cross section

Converting the PD relative cross section in arbitrary units (A.U.) into absolute PD cross section (Å^2) is done by comparing our new data to the absolute cross section measurements in the VDE region (3.626 -4.15eV) made by Mock et al.[30] The simultaneous measurement of SF$_6^-$ together with the other cluster anion species under the same experimental conditions allows to determine the absolute cross section for all the measured ions.

5. Results and discussion

In figure 18 we show the decay of the trapped ions as a function of trapping time, measured using the pickup method. The life time for the decaying ions is mostly composed of 2 exponents and shown at table 1. For $(SF_6)_{n=1,2,3}$ the life time is shorter than expected from former experiments and could not be compared to them, due to comparable high RF voltage (10V compare to 4V). The high RF voltage was used for making a better bunching, but it is also known for pushing ions out of the EIBT.[42]

$(SF_6)_{13}^-$ decay occurs also from black body induced dissociation (BIRD).[47] The number of ions at short times does not reflect their relative production efficiency as in figure 9, as we intentionally limit the number of ions injected into the trap, minimizing the probability of MCP readout saturation.

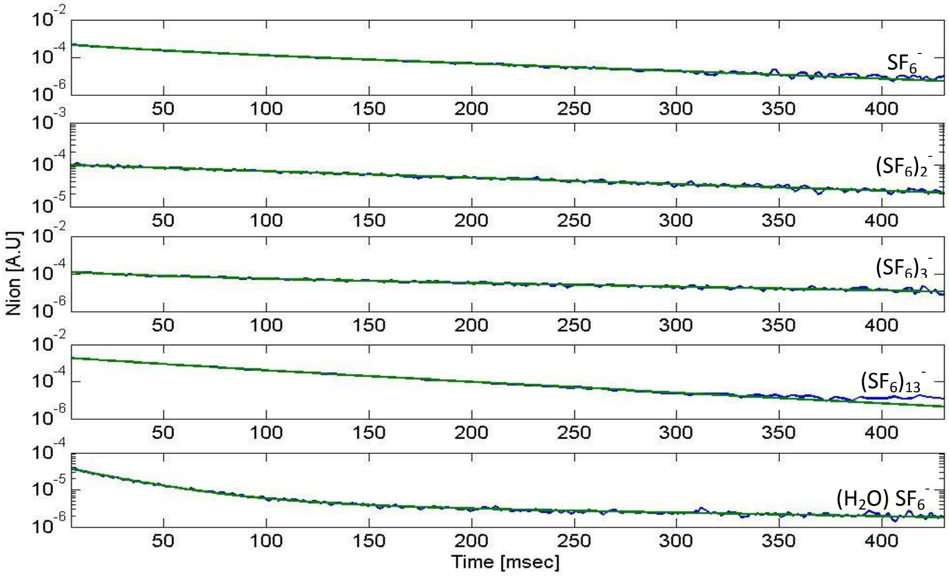

Figure 18: Number of ions in the EIBT (the blue line) exponentially decaying and the fit (in green) for each desired cluster.

	1^{st} coefficient	1^{st} life time	2^{nd} coefficient	2^{nd} life time
SF_6^-	$(212 \pm 13) * 10^{-6}$	31±2ms	$(295 \pm 14) * 10^{-6}$	107±3ms
$(SF_6)_2^-$	$(99 \pm 1) * 10^{-6}$	279±5ms		
$(SF_6)_3^-$	$(80 \pm 7) * 10^{-6}$	219± 16 ms	$(49 \pm 60) * 10^{-6}$	38±9 ms
$(SF_6)_{13}^-$	$(1290 \pm 600) * 10^{-6}$	76±10ms	$(739 \pm 583) * 10^{-6}$	40±14 ms
$(H_2O)\ SF_6^-$	$(5 \pm 1) * 10^{-6}$	449±49 ms	$(36 \pm 1) * 10^{-6}$	35±1 ms

Table 1: Showing results of life time fitting for the different ions, using $Ae^{-t/\tau_1} + Be^{-t/\tau_2}$.

Figure 19 shows the MCP from RG collisions only, averaged for ~1500 trapping cycles for each ion mass. The signal (N_{mcp}) is predominantly due to neutralization by ion collisions with the residual gas and is related to the N_{ions} - the number of trapped ions by:

$$N_{mcp}(t) = \eta k N_{ions}(t) dt \tag{12}$$

Where N_{mcp} is the number of hits on the MCP in a dt long time window, η is the detection efficiency of the detector and k is the neutralization rate constant. These average hit rates are subtracted as background to the photodetachment process.

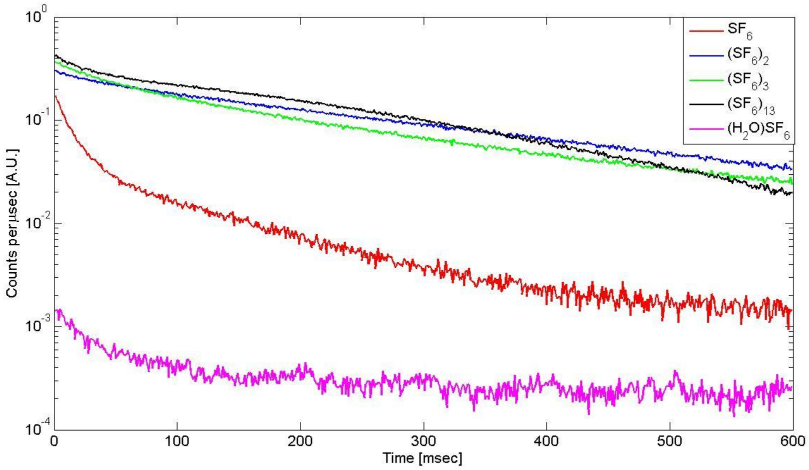

Figure 19: Neutrals fragments detected by the MCP of $(SF_6)^-_{n=1,2,3,13}$ and $(H_2O)SF_6^-$ due to residual gas collision.

Figure 20 shows the N_{mcp}/N_{ion} . Although the ratio stays stable as a function of trapping time for SF_6, $(SF_6)_2$, and $(SF_6)_3$, it cannot be used as a relative measure of the number of anions as the neutralization rate k is different for the different ions as can be seen in figure 20. For $(SF_6)_{13}$ we see an increase, the reason for that is that $(SF_6)_{12}^-$ products are close enough in energy to the 4.2keV parent anion and can stay trapped in the EIBT. The decay of these accumulated daughter ions also produces counts on the MCP at later times in addition to the signal from the parent anion neutralization signal. However, the $(SF_6)_{12}^-$ ions oscillate at a different frequency and are not synchronized by the RF potential and are undetected by the pickup, explaining the increase of N_{MCP} / N_{ion} ratio. Neutral detection window, shown in figure 14, helps screen some of the $(SF_6)_{12}^-$ background in the $(SF_6)_{13}^-$ measurements. Nevertheless, we have less confidence in the absolute photodetachment cross section we derive for the large cluster. Another parameter important to notice is the paper written by G.W. Fraser[52] that shows that from a certain small energy hit on the detector, the efficiency of the MCP decreases. Since the $(SF_6)_{13}^-$ fragments can dissociate to $(SF_6)_{12}^-$ +SF_6, the SF_6 may have low energy and detected with smaller efficiency by the MCP.

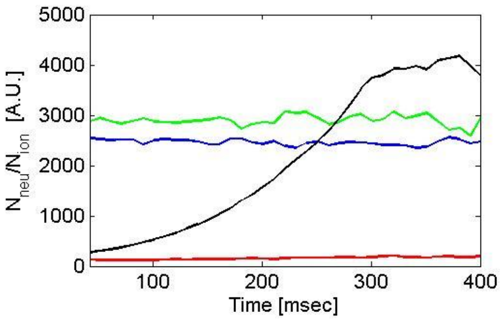

Figure 20: Ratio of N_{mcp} by N_{ion}. SF_6^- , $(SF_6)_2^-$ and $(SF_6)_3^-$ (red, blue and green respectively) ratios is stable while $(SF_6)_{13}^-$ ratio (black) change due to $(SF_6)_{12}^-$ daughter clusters that may be trapped by the EIBT and hit the MCP but are not detected by the pickup due to different frequency oscillation.

Figure 21 shows a zoomed in view around the time of the laser pulse for the measured ions. For SF_6^- the periodic average background signal is so low that it is not detected under our good UHV conditions. For the clusters $(SF_6)_{n=2,3,13}^-$ an ion bunch is observed to be in a very good synchronization with the laser shot. Furthermore, the averaged BG stayed the same before and after the laser hit, implying only a small change had happened to the total number of ions inside the EIBT. The number of trapped $(H_2O)SF_6^-$

ions is small, also leading to a nearly undetectable RG background signal. It is important to distinct between neutralization that happens from photons to neutralizations that happens from RG hits. Whereas the photodetachment occurs from laser interaction with the SF_6^- molecule, even if it's embedded inside a cluster, RG signal reflects the collision cross section of the entire cluster. Indeed, as can be seen in figure 21, there is relatively more RG counts in the MCP for the clusters compared to the molecular anion.

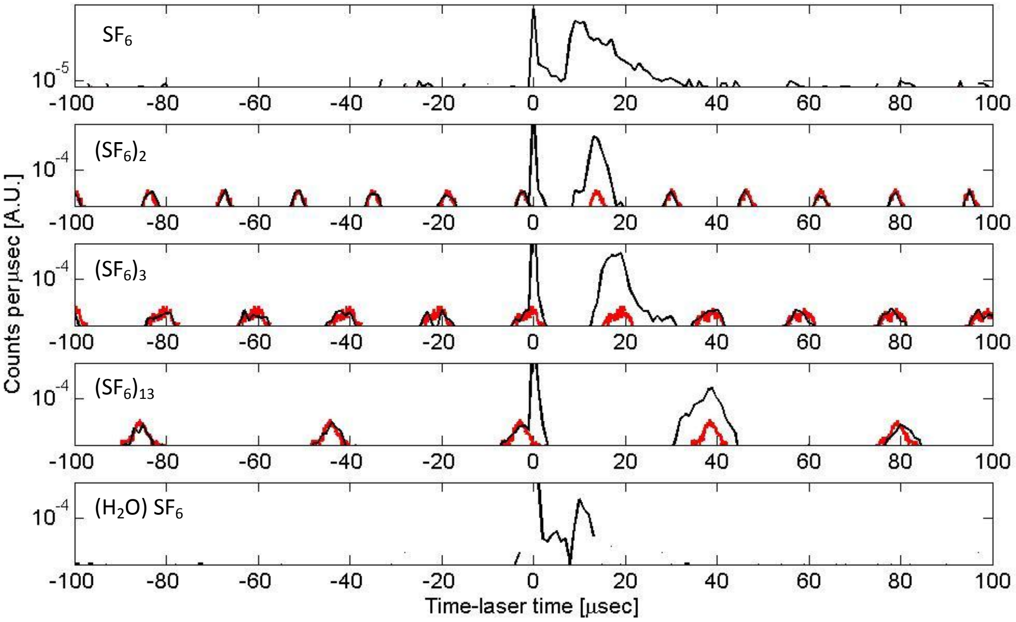

Figure 21: Zoom in around the laser time for the different ions (in black). The raw data is an average of about ~1500 measurements. When after synchronization, the ions-laser photodetachment neutral signal comes with the residual gas neutral signal. The number of trapped $(H_2O)SF_6^-$ ions is small, also leading to a nearly undetectable RG background signal. We can see background before and after (in red) the laser shot and that it did not change the number of ions in the EIBT. Background put on the laser-ion overlap fragments show a good timing synchronization between the laser and the ion bunch.

Figure 22 shows SF_6^- PD relative cross section curve after normalization to Mock et al[30] (in red). The results are compared to integral over Eisfeld[17] calculations (dashed blue line) as shown in equation 4. Measurements of Datskus et al[53] are not shown as they fall in the gap of the tunable laser, preventing a direct comparison to the new data presented here.

For SF_6^-, we extend previous cross section measurements by more than 1eV towards the adiabatic limit, by reaching more than 2 order of magnitude improvement in measurement sensitivity. The calculated cross section clearly does not fit the shape of the measured PD cross section. We fitted the experimental cross section by using the calculated FC overlaps, albeit shifting ADE value. The full blue line shows the best fit obtained for a shift of 0.77eV fitting the measured data over several orders of magnitude cross section change. This shift suggests that a significantly higher ADE of ~1.7eV would be in agreement with our PD cross section measurements.

The shape of the measured curve cannot be well represented by fitting with simple threshold Wigner threshold law of the $(\mathrm{E}-\mathrm{ADE})^{\frac{2l-1}{2}}$ often used in analysis of near threshold photoionization and PD data.[62,66] Interestingly, a $\sigma_{PD} \propto (1-ADE/h\nu)^{1/2}$ phenomenological threshold law sometimes applied in astrophysics[65] successfully fits the data below 3eV with an ADE = 1.7 ± 0.02 eV. The fitted phenomenological threshold law curve is not shown as it practically indistinguishable from the calculated blue solid curve in figure 22. Indeed, the steep PD cross section drop combined with the reduced laser power at the lower photon energies prevented a direct measurement of the inefficient PD transition to the vibrational ground state at ADE photon energy. Nevertheless, the agreement over several orders of magnitude between the measured data and the calculated cross-section is remarkable.

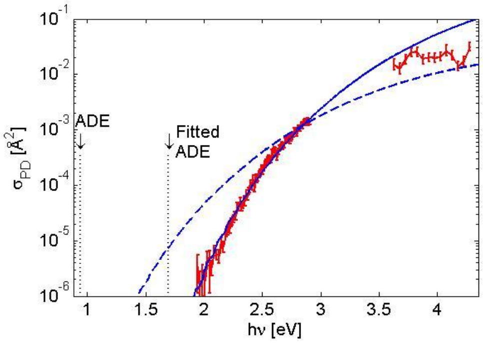

Figure 22: SF_6^- experimental cross section (red line) with Eisfeld[17] adjusted theoretical calculations (dashed blue line) and shifted of the calculations (blue line) to fit experimental results. ADE calculated by Eisfeld to be 0.9eV is suggested from the shifting to be 1.7eV. Phenomenological threshold law gave same exact results.

Measurements of PD cross section and relative cross section for $(SF_6)_n^-$ small cluster ions are shown in the next figures.

Figure 23 shows mean cross section around 2.7eV for $(SF_6)_{n=1\text{-}3}^-$. One can easily see that the cross section stays the same within the experimental error bars. Together with the simulation done by Luzon[54] and shown earlier in figure 7, we conclude that the electron stays localized on a single SF_6 and does not spread over the cluster. Such delocalization is expected to decrease the equilibrium S-F bond length, which in turn is expected to strongly increase the PD cross section in the near ADE region. $(SF_6)_{13}^-$ is not included in this comparison as we have concerns about our absolute detection efficiency of small fragments of the clusters.

	SF_6^-	$(SF_6)_2^-$	$(SF_6)_3^-$
$\sigma_{PD}@2.7eV$	$(6.4\pm1.3)*10^{-4}\text{Å}^2$	$(8.5\pm1.7)*10^{-4}\text{Å}^2$	$(4.3\pm1.1)*10^{-4}\text{Å}^2$

Table 2: Mean cross section of SF_6^-, $(SF_6)_2^-$, and $(SF_6)_3^-$ around 2.7eV.

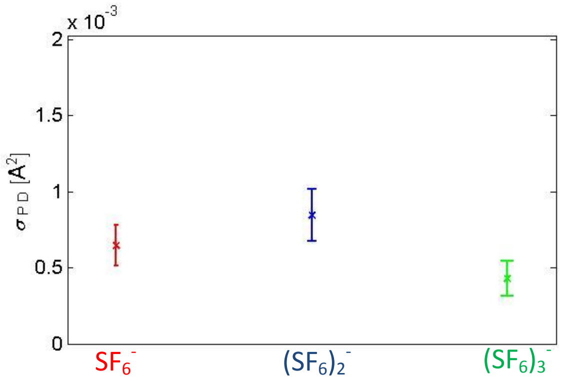

Figure 23: Mean cross section around 2.7eV is shown for $(SF_6)^-$, $(SF_6)_2^-$ and $(SF_6)_3^-$.

Figure 24 shows the PD relative cross section curves of SF_6^-, $(SF_6)_2^-$,$(SF_6)_3^-$ and $(SF_6)_{13}^-$ with the blue reference lines of the adjusted Eisfeld culculations fitted for SF_6^-. The fit was normalized from SF_6 to the other clusters at 2.7eV and from the comparably same shape of the ions and the explanation we strengthened the conclusion that charge is localized on a single SF_6^- at each cluster.

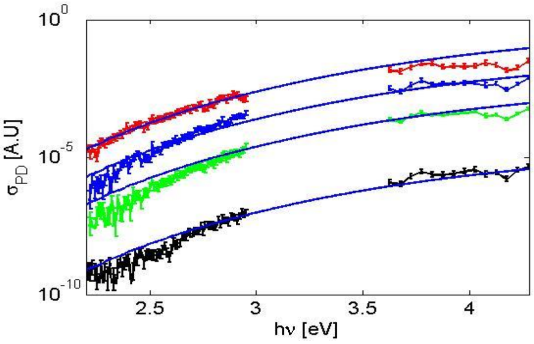

Figure 24: Normalized PD relative cross sections of SF_6^-, $(SF_6)_2^-$, $(SF_6)_3^-$ and $(SF_6)_{13}^-$ to different heights (red, blue, green, black respectively), and the adjusted Eisfeld calculations (black) comparing to each molecule.

Although the clusters exhibit very similar cross section shapes, we notice small differences in cluster anions PD cross section at the low energy tails. The clusters exhibit lower PD cross section although charge delocalization would account for exactly the opposite – an increase of cross section in the near ADE region due to reduced S-F bond elongation. Figure 25 is showing harmonic oscillator PD relative cross section model calculated by Itamar Luzon[54], with equilibrium bond length of 1.70Å, ADE=1eV in zero temperature comparing to room temperature of the anion. The molecular anion is stable at room temperature, while the cluster anions are weakly bound against evaporation and can only be formed in the cold expansion source. It is therefore possible that the higher tail of the molecular anion comes from vibrationally hot molecules.

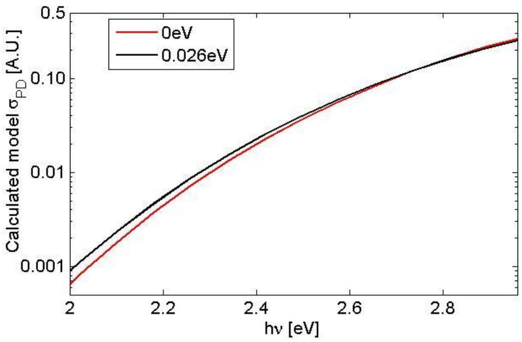

Figure 25: Numerical calculated PD relative cross section of harmonic oscillator with equilibrium bond length of 1.70Å, ADE=1eV in zero temperature (red) comparing to room temperature (black).

In a preliminary attempt to quantify the observed changes between the different clusters we used the same ADE fitting procedure described for SF_6^-, for the cluster anions. The fitted ADE values, all with R^2 higher than 0.99, are summarized in table 3. The higher errorbars reflect the lower statistics for the less abundant cluster anions – further measurements focusing on the low photon energy points will improve this comparison. In any case, a small change between the molecule and cluster anions is evident possibly reflecting a small residual fraction of hot molecular anions.

	SF_6^-	$(SF_6)_2^-$	$(SF_6)_3^-$	$(SF_6)_{13}^-$
ADE	1.7±0.02eV	1.9±0.04eV	1.9±0.06eV	2±0.12eV

Table 3: The fitted ADE with R^2 >0.99 for SF_6^-, $(SF_6)_2^-$, $(SF_6)_3^-$ and $(SF_6)_{13}^-$.

Figure 26 is comparing between preliminary PD cross section measurements of SF_6^- and $(H_2O)SF_6^-$. The clear differences between SF_6 and $(H_2O)SF_6$ cross section shapes may indicate that H-bond in $(H_2O)SF_6$ increases the vertical detachment energy by further distortion of the SF6- anion structure and stabilization of the excess electron.

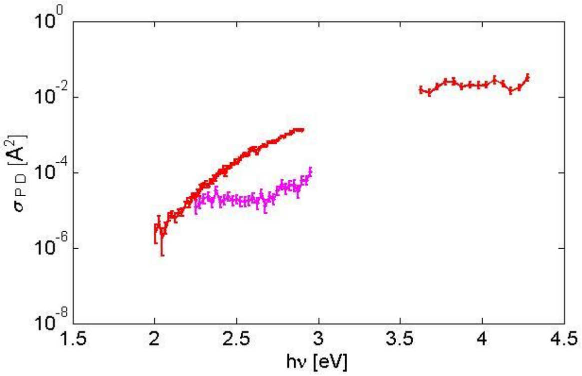

Figure 26: SF_6^- PD cross section (red line) and $(H_2O)SF_6^-$ PD cross section (magenta line) .

6. Summery and Conclusions

I presented photodetachment measurements of cold SF_6^- and small SF_6^- based cluster anions that were performed using an EIBT, allowing highly sensitive measurements of PD cross sections down to the 10^{-6}Å^2 scale.

For SF_6^-, the new data extends the previously reported PD cross section measurements by more than an eV towards lower photon energies, approaching the ADE threshold limit. Fitting the measured shape of the steep cross section drop over more than 3 orders of magnitude with either a phenomenological threshold law function,[65] or with theoretically calculated FC overlaps,[22] allows extraction of SF_6^- ADE values of 1.7 ± 0.02 eV, significantly higher than the presently accepted experimental estimates that are based on electron attachment and electron detachment kinetics modelling.[67] As both experimental approaches rely on theoretically calculated inputs in order to extract ADE values, we propose that further theoretical work is required to resolve the apparent discrepancy. For example, by providing improved SF_6^- anion vibrational ground state wave function calculation in the overlap region that accounts for the observed steep cross section drop, while maintaining lower ADE. Or alternatively by providing theoretical description of either bound or dissociative excited anion states that may alter the interpretation of the experimental data.

The absolute cross section of SF_6^-, $(SF_6)_2^-$ and $(SF_6)_3^-$ at ~2.7eV is shown to be the same, where for the SF_6^- the cross section is $(6.5 \pm 1.3)*10^{-4}\text{Å}^2$ and $(SF_6)_2^-$ and $(SF_6)_3^-$ cross sections are overlapping with it within the errorbars. As photodetachment cross section below the VDE is expected to be extremely sensitive to the equilibrium S-F bond length, we conclude that S-F bond length is not affected by the additional SF_6 units and that charge delocalization similar to the one found in cationic rare gas clusters in unlikely. $(SF6)_n^-$ PD cross section curve shape is found to be similar to that of SF_6^-. In contrast to the extended tail towards low photon energies that one could predict in case of S-F bond shrinking due to charge delocalization in clusters, a slightly longer tail is observed below 2.3eV for SF_6^- compared to the cluster anions. We tentatively interpret this tail as due to small fraction of hot molecular anions that is not possible for the loosely bound cluster anions.

Expanding capabilities toward working with microsolvated systems, we report preliminary PD cross section measurement for $(H_2O)SF_6^-$ in the 1.76-2.95eV photon energy range. Preliminary data suggests the possibility of excess electron stabilization by H-bond formation. However further work is needed, including planned experiments in the higher photon energy range and with additional water units.

7. References

1. P.G. Ashbaugh,D.W. McAdam, and M. F. J. SF_6 - its propeties and use as a gaseous insulator in Van De Graaff accelerators. *IEEE Trans. Nucl. Sci.* 266 (1965).

2. Newell, W. M. J. and W. R. Absolute elastic differential cross sections for electron scattering from SF_6. *J. Phys. E At. Mol. Opt. Phys.* 24, 473–487 (1991).

3. Qureshi, N. H. Mi. and A. H. A reveiw of electrical breakdown in mixtures of SF_6 and other gases. *IEEE Trans. Electr. Insul* EI-14, 1 (1979).

4. Hussain, S. Q. *et al.* Light trapping scheme of ICP-RIE glass texturing by SF6/Ar plasma for high haze ratio. *Vacuum* 94, 87–91 (2013).

5. Gharooni, M. *et al.* A novel non-sequential hydrogen-pulsed deep reactive ion etching of silicon. *J. Micromechanics Microengineering* 23, 095014 (2013).

6. Cheng, J.-H., Bartos, S. C., Lee, W. M., Li, S.-N. & Lu, J. (Ching-H. SF_6 usage and emission trends in the TFT-LCD industry. *Int. J. Greenh. Gas Control* 17, 106–110 (2013).

7. Ko, M. K. W. *et al.* Atmospheric Sulfur Hexafluoride ' Sources , Sinks and Greenhouse Warming. 98, (1993).

8. Reddmann, T., Ruhnke, R. & Kouker, W. Three-dimensional model simulations of SF_6 with mesospheric chemistry. *J. Geophys. Res.* 106, 14525 (2001).

9. Houghton, et al. GWPs and atmospheric lifetimes of halocarbons and other halogenated compounds. *IPCC SAR* (1996). at <http://www.ipcc.ch/ipccreports/sres/emission/index.php?idp=123>

10. Rigby, M. *et al.* History of atmospheric SF_6 from 1973 to 2008. *Atmos. Chem. Phys.* 10, 10305–10320 (2010).

11. Brenninkmeijer, C. A. M. Atmospheric SF_6 : Trends , Sources , and Prospects. *Environ. Sci. Technol* 32, 3077–3086 (1998).

12. Troe, J., Miller, T. M. & Viggiano, A. A. Communication : Revised electron affinity of SF_6 from kinetic data Communication : Revised electron affinity of SF_6 from kinetic data. *1. Troe J, Mill. TM, Viggiano AA. Commun. Revis. electron Affin. SF6 from Kinet. data Commun. Revis. electron Affin. SF_6 from Kinet. data. 2012;1211021–4.* 136, 121102 (2012).

13. Compton, R. N., Reinhardt, P. W. & Cooper, C. D. Collisional ionization between fast alkali atoms and selected hexafluoride molecules. *J. Chem. Phys.* 68, 2023 (1978).

14. Streit, G. E. Negative ion chemistry and the electron affinity of SF_6. *J. Chem. Phys.* 77, 826 (1982).

15. Chen, E. C. M., Wiley, J. R., Batten, C. F. & Wentworth, W. E. Determination of the electron affinities of molecules using negative ion mass spectrometry. *J. Phys. Chem.* 98, 88–94 (1994).

16. Viggiano, A. A., Miller, T. M., Friedman, J. F. & Troe, J. Low-energy electron attachment to SF6 . III . From thermal detachment to the electron affinity of SF_6. *J. Chem. Phys.* 127, 244305 (2007).

17. Eisfeld, W. Highly accurate determination of the electron affinity of SF_6 and analysis of structure and photodetachment spectrum of SF_6^-. *J. Chem. Phys.* 134, 054303 (2011).

18. Gerchikov, L. G. & Gribakin, G. F. Electron attachment to SF_6 and lifetimes of SF_6^- negative ions. *Phys. Rev. A* 77, 042724 (2008).

19. Appelhans, A. D. & Delmore, J. E. Refinement of the autoneutralization lifetimes of short lived states of SF−6. *J. Chem. Phys.* 88, 5561 (1988).

20. Liu, Y., Suess, L. & Dunning, F. B. Rydberg electron transfer to SF_6 : Product ion lifetimes. *J. Chem. Phys.* 122, 214313 (2005).

21. Rajput, J., Lammich, L. & Andersen, L. H. Measured Lifetime of SF_6^-. *Phys. Rev. Lett.* 100, 153001 (2008).

22. Borrelli, R. Franck – Condon analysis of the SF_6^- electron photodetachment spectrum. *Chem. Phys. Lett.* 445, 84–88 (2007).

23. Gutsev, G. & Bartlett, R. Adiabatic electron affinities of PF5 and SF_6: a coupled-cluster study. Mol. Phys. 94, 121-125 (1998).

24. Bopp, J. C. *et al.* Spectroscopic Characterization of the Isolated SF_6^- and $C_4F_8^-$ Anions : Observation of Very Long Harmonic Progressions in Symmetric Deformation Modes upon Photodetachment. *J. Phys. Chem. A* 111, 1214–1221 (2007).

25. McMillen, D. F. & Golden, D. M. Hydrocarbon Bond Dissociation Energies. *Annu. Rev. Phys. Chem.* 33, 493–532 (1982).

26. Wang, Y., Champion, R. L., Doverspike, L. D., Olthoff, J. K. & Van Brunt, R. J. Collisional electron detachment and decomposition cross sections for SF_6^-, SF_5^-, and F^- on SF_6 and rare gas targets. *J. Chem. Phys.* 91, (1989).

27. Fehsenfeld, F. C. Electron Attachment to SF6. *J. Chem. Phys.* 53, (1970).

28. Avrillier, S. & Schermann, J.-P. Vibrational excitation of SF_6 by electron impact. *Opt. Commun.* 19, 87–91 (1976).

29. Gutsev, G. L. THE STRUCTURE OF THE SF 6 MOLECULE AND THE SF_6^- ANION EXCITED STATES G. L. Gutsev. *Inst. Chem. Physics, Russ. Acad. Sci.* 5622, 504–510 (1992).

30. Mock, R. S. & Grimsrud, E. P. Electron photodetachment of the molecular anions of SF_6 and several perfluorinated hydrocarbons. *Chem. Phys. Lett.* 184, 99–101 (1991).

31. Ingólfsson, O. & Wodtke, A. Bridging the Cluster-to-Bulk Divide: Electron Attachment Time-of-Flight Mass Spectrometry Reveals Geometrical Shell Closings in $(SF_6)_n$ Clusters (n=2 – 550). *Phys. Rev. Lett.* 87, 183401 (2001).

32. Ingolfsson, O. & Wodtke, A. M. Electron attachment time-of-flight mass spectrometry reveals geometrical shell closings in van der Waals aggregates. *J. Chem. Phys.* 117, 3721 (2002).

33. Haberland, H. *et al.* Electronic and Geometric Structure of Ar_n^+ and Xe_n^+ Clusters: The Solvation of Rare-Gas Ions by Their Parent Atoms. *Phys. Rev. Lett.* 67, 3290–3293 (1991).

34. Gascón, J. a., Hall, R. W., Ludewigt, C. & Haberland, H. Structure of Xe_n^+ clusters (N=3–30): Simulation and experiment. *J. Chem. Phys.* 117, 8391 (2002).

35. Even, U., Jortner, J., Noy, D., Lavie, N. & Cossart-Magos, C. Cooling of large molecules below 1K and He clusters formation. *J. Chem. Phys.* 112, 8068 (2000).

36. Zajfman, D. *et al.* Electrostatic bottle for long-time storage of fast ion beams. *Phys. Rev. A* 55, R1577–R1580 (1997).

37. Strasser, D. *et al.* Negative Mass Instability for Interacting Particles in a 1D Box: Theory and Application. *Phys. Rev. Lett.* 89, 283204 (2002).

38. Pedersen, H. *et al.* Diffusion and synchronization in an ion-trap resonator. *Phys. Rev. A* 65, 042704 (2002).

39. Andersen, L. H., Heber, O. & Zajfman, D. Physics with electrostatic rings and traps. *J. Phys. B At. Mol. Opt. Phys.* 37, R57–R88 (2004).

40. Toker, Y. *et al.* The kick-out mass selection technique for ions stored in an Electrostatic Ion Beam Trap. *J. Instrum.* 4, P09001–P09001 (2009).

41. EKSPLA, Tunable Nd:YAG-Laser System NT342B-SH.

42. Rahinov, I., Toker, Y., Heber, O., Strasser, D. & Rappaport, M. Lifetime measurements in an electrostatic ion beam trap using image charge monitoring. *Rev. Sci. Instrum.* 83, 033302 (2012).

43. WIZA, J. L. Microchannel plate detectors. *Nucl. INSTRUMENTS METHODS* 162, 587–601 (1979).

44. Matsuura, S., Umebayashi, S., Okuyama, C. & Oba, K. Characteristics of the Newly Developed MCP and Its Assembly. *IEEE Trans. Nucl. Sci.* 32, 350–354 (1985).

45. Heber, O. *et al.* Electrostatic ion beam trap for electron collision studies. *Rev. Sci. Instrum.* 76, 013104 (2005).

46. Naaman, R. & Vager, Z. An electron multiplier capable of working at low vacuum: The microsphere plate. *Rev. Sci. Instrum.* 67, 3332 (1996).

47. Toker, Y. *et al.* Blackbody-induced radiative dissociation of cationic SF6 clusters. *Phys. Rev. A* 86, 023202 (2012).

48. Attia, D., Strasser, D., Heber, O., Rappaport, M. L. & Zajfman, D. Transverse kinematics of ions stored in an electrostatic ion beam trap. *Nucl. Instruments Methods Phys. Res. Sect. A Accel. Spectrometers, Detect. Assoc. Equip.* 547, 279–286 (2005).

49. Straub, H. C., Mangan, M. a., Lindsay, B. G., Smith, K. a. & Stebbings, R. F. Absolute detection efficiency of a microchannel plate detector for kilo-electron volt energy ions. *Rev. Sci. Instrum.* 70, 4238 (1999).

50. Strasser, D. *et al.* Tunable wavelength soft photoionization of ionic liquid vapors. *J. Phys. Chem. A* 114, 879–83 (2010).

51. Holger Schneider and J.Mathias Weber.Infrared spectra of S F 6 (H 2 O) n (n = 1 – 3) :Incipient reaction and delayed onset of water network formation. *J. Phys. Chem.*127, 244310 (2007);

52. G.W. Fraser. The ion detection efficiency of microchannel plates (MCPs). *International Journal of Mass Spectrometry 215 (2002) 13–30*

53. P.G. Datskos, J.G. Carter, L.G. Christophorou. Photodetachment of SF_6^-.Chemical Physics Letters 239 38-43 (1995).

54. Itamar Louzon thesis, Supervisor: Daniel Strasser. The Hebrew University of Jerusalem (2013).

55. O. Echt, K. Sattler, and E. Recknagel. Magic Numbers for Sphere Packings: Experimental Verification in Free Xenon Clusters. Phys. Rev. Lett. 47, 1121 (1981).

56. T. Martin. Shells of atoms. Phys. Rep. 273, 199 (1996).

57. O. Ingolfsson and A. M. Wodtke, J. Chem. Phys. 117, 3721 (2002).

58. John L Bullister, David P Wisegarver and Frederick A Menzia. The solubility of sulfur hexafluoride in water and seawater. Deep Sea Research Part I: Oceanographic Research Papers. vol.49 (2002)

59. Susan T. Arnold and A. A. Viggiano. Turbulent Ion Flow Tube Study of the Cluster-Mediated Reactions of SF6- with H2O,CH3OH, and C2H5OH from 50 to 500 Torr. J. Phys. Chem. A 105 (2001)

60. Y. Toker, I. Rahinov, D. Schwalm, U. Even, O. Heber, M. L. Rappaport, D. Strasser and D. Zajfman. Blackbody-induced radiative dissociation of cationic SF6 clusters. PHYSICAL REVIEW A 86, 023202 (2012)

61. Kenzo Hiraoka, Akitaka Shimizu, Akihito Minamitsu, Masayuki Nasu, Susumu Fujimaki, Shinichi Yamabe. The small binding energies of the negative cluster ions: $SF_5^-(SF_6)_1$, $SF_6^-(SF_6)_1$ and $F^-(SF_6)_n$ (*n* = 1 and 2), in the gas phase. Chemical Physics Letters. 241(1995)

62. E.P. Wigner. On the behavior of cross section s near thresholds. Phys.Rev 73, 1002 (1948)

63. L.G. Chrisophorou. Electron interactions with SF6. J. Phys. Chem. Ref. Data29 267 (2000)

64. H. Pedersen, D. Strasser, B. Amarant, O. Heber, M. Rappaport, and D. Zajfman. Stability and loss in an ion-trap resonator. *Phys. Rev. A* 65, 042704 (2002) .

65. T. J. Millar, C. Walsh, M. A. Cordiner, R. N. Chuimın, and E. Herbst, *Astrophys. J.*. 662 (2007)

66. J. W. Farley. Photodetachment cross sections of negative ions: The range of validity of the Wigner threshold law. *Phys. Rev. A* 40 (1989)

67. Troe J, Miller TM and Viggiano AA. Communication: Revised electron affinity of SF6 from kinetic data. J. Chem. Phys. 136 (2012)

מבוא

עבודת התזה המוצגת כאן עוסקת במדידה של חתך הפעולה של פוטו-הוצאת אלקטרון מ- SF_6^-, מצבירים יונים קטנים של SF_6^- ומ- $(H_2O)SF_6^-$. המדידה של חתך הפעולה של פוטו-הוצאת האלקטרון מ- SF_6^- כפונקציה של אנרגית הפוטונים בתווך של 210-355nm ו 420-705nm , מושווית לעבודה חישובית המבוססת על חפיפת Frank-Condon מסביבת רמת היסוד ההתחלתית לרמות האנרגיה של SF_6 הנייטראלי, לפי המעברים המותרים. על ידי הוספה של הזזה לחישוב אנרגיית ההוצאה האדיאבטית (ADE), החישוב והמדידות חופפים על פני שלושה סדרי גודל של חתך הפעולה כגד אנרגיית הפוטון. ההשוואה ביניהם נותנת ערך ADE של ~ 1.7 ±0.02eV, שיוצא יותר גבוה מהערך המקובל היום של 1eV. כמו כן, עבור הצבירים הקטנים מבוססי SF_6, נעשה דיון בהבדלים הקטנים שנמצאו בחתך הפעולה של הפוטו-הוצאת אלקטרון מ- $(SF6)_n^-$ כאשר n=2,3,13.

האוניברסיטה העברית בירושלים
The Hebrew University of Jerusalem

הפקולטה למתמטיקה ולמדעי הטבע,

קמפוס אדמונד דה ספרא (גבעת רם),

המחלקה לכימיה

מדידת חתך הפעולה לתלישת אלקטרון של SF_6^- וצבירים אניונים קטנים מבוססי $(SF_6)_n^-$

עבודת מחקר לשם קבלת תואר מוסמך

בכימיה פיזיקלית

מעוז נגלר

ת.ז. 021587019

מנחה: ד"ר דניאל סטראסר

כסלו תשע"ה

דצמבר 2014